

# HIGH-PRECISION POINTING PLATFORM PERFORMANCE SIMULATIONS FOR SMALL SPACECRAFT MISSIONS

W. De Munter<sup>(1)</sup>, J. De Maeyer<sup>(1)</sup>, L. Peri<sup>(1)</sup>, D. Vandepitte<sup>(1)</sup>

<sup>(1)</sup>*KU Leuven, Celestijnenlaan 300, wim.demunter@kuleuven.be*

## ABSTRACT

Vibrations deteriorate the image quality of satellite's onboard optical instruments. One of the solutions to improve the image quality is to actively compensate for these vibrations by means of a dual-stage control approach. While this approach is common for large spacecraft (> 100 kg), several challenges arise when it is applied on small spacecraft (< 10 kg). This paper explains a dual-stage control approach with precise actuators and accurate sensors for both an astronomy and an Earth Observation mission. The pointing performance is evaluated by means of time-domain simulation models. The result show that, compared to single-stage pointing control, the proposed dual-stage control approach can improve the pointing performance by more than 50% for an astronomy mission with an optical payload. For smallsat EO missions, simulations show the importance of an accurate gyroscope for optimal performance. Finally, several recommendations are proposed based on the simulation results.

## 1 INTRODUCTION

High-quality data from space are the key source for the next-generation application developments and science discoveries. In the field of astronomy, high-quality data allows scientist to make new discoveries to better understand our solar system and the galaxy, while in the field of Earth Observation (EO), high-quality data will play a very important role in sustainability development areas such as monitoring the environment, assisting circular economy, land protection, smart cities, disaster and emergency responses, ...

Today, high-quality data are typically acquired from large and expensive spacecraft platforms (> 500 kg), as they can be equipped with powerful and sophisticated hardware instruments. The obtained imagery, however, is not affordable and has a low temporal resolution due to the long revisit times. To tackle both shortcomings, small spacecraft (< 50 kg) could be the answer. Building large constellations of small standardized satellites, can provide global coverage with high temporal resolution and affordable imagery. Within the field of small spacecraft, a particular booming class are CubeSats. A one-unit (1U) CubeSat is a small satellite with standardized dimensions of  $10 \times 10 \times 10 \text{ cm}^3$ , a mass of about 2 kg, and a power consumption of approximately 1 W [1]. By combining several of these 1U cubes, derivatives such as 3U, 6U and 12U CubeSats can be obtained. The main success of CubeSats can be assigned to this standardized concept in combination with the use of Commercial-Off-The-Shelf (COTS) components, leading to a reduction in development time and cost, and to affordable access into space [2].

One of the main challenges with small satellites is to maintain the high-quality standard of the data as acquired from large spacecraft platforms. First, the limited volume and power budget make it

difficult to install large and/or power-consuming instruments, although this could be largely resolved by technology miniaturisation and deployable structures. Secondly, the inherent low spacecraft's inertia make it difficult to stabilize the platform by means of the Attitude Determination & Control Subsystem (ADCS).

## 1.1 Pointing performance

The ADCS determines and controls the spacecraft's orientation, or *attitude*. Different types of sensors, of which the star tracker (ST) is typically the most accurate one, measure and estimate the attitude, while different types of actuators, of which the reaction wheels (RW) are typically the most agile ones, control the attitude. The performance of this closed-loop control ADCS subsystem can be expressed according to the ECSS standards [3]. The three pointing performance metrics used in the remainder of the paper are:

- Absolute Pointing Error (APE): the pointing error between the actual and desired attitude.
- Relative Pointing Error (RPE): the pointing error between the actual and mean attitude over a certain time window.
- Absolute Knowledge Error (AKE): the knowledge error between the actual and estimated attitude.

The APE of a CubeSat ADCS typically reaches its limit at around  $0.03^\circ$  ( $3\sigma$ ) [4], which is not sufficient to provide high-quality images. Although the star tracker is able to estimate the attitude very accurately, in the range of 20 arcsec cross-boresight, the reaction wheels are typically too slow to counteract small, high-frequency ( $> 10$  Hz) micro-vibrations, also called *jitter*, that cause images to be blurry. These high-frequency vibrations typically originate from the reaction wheels itself [5]. Passive solutions, such as dampers, exist to minimize the vibrations before reaching the optical instrument. However, these dampers can be tuned only for a limited frequency bandwidth, while the disturbances generated by reaction wheels span a large frequency range as these actuators continuously change their rotation speed. An alternative solution is to actively compensate for these vibrations by means of a dual-stage control approach, in which the ADCS counteracts the low-frequency vibrations ( $< 1$  Hz) and a so-called high-precision pointing platform (HPPP) copes with the mid- to high-frequency vibrations ( $> 10$  Hz).

## 1.2 Dual-stage control design approach

The dual-stage control approach has been already applied to space missions in the past. A comparative study of some CubeSats with and without active optics can be found in [6]. Table 1 lists their pointing performance and clearly indicates the added value of active components with respect to the features of pointing performance. Apart from active optics, the main drivers of pointing performance are the onboard reaction wheels and the kind and quality of the sensors used to determine the spacecraft's attitude. The dual-stage control strategy (ADCS + HPPP) presented in this paper is illustrated in Figure 1. The outer loop represents the ADCS with a star tracker as the most accurate sensor and reaction wheels as the most agile actuators. A Multiplicative Extended Kalman Filter (MEKF) in the form of a gyro-stellar estimator is considered, as well as a simple Proportional-Integral-Derivative (PID) attitude control algorithm. The inner loop represents the HPPP, mainly acting on the payload optics, with a fine-steering mirror (FSM) and a dedicated optical sensor as the main actuator and sensor respectively. This second control stage aims at increasing the bandwidth of the entire pointing system by counteracting higher frequency disturbances as well.

Table 1: Overview of different CubeSat missions with an optical payload and with or without active optics [6].

CubeSat	Active optics	Pointing Performance [arcsec]
UniBRITE	No	45.0 (rms)
BRITE-Toronto	No	11.8 (rms)
ASTERIA	Yes	2.3 ( $3\sigma$ )
PicSat	Yes	1.41 ( $3\sigma$ )

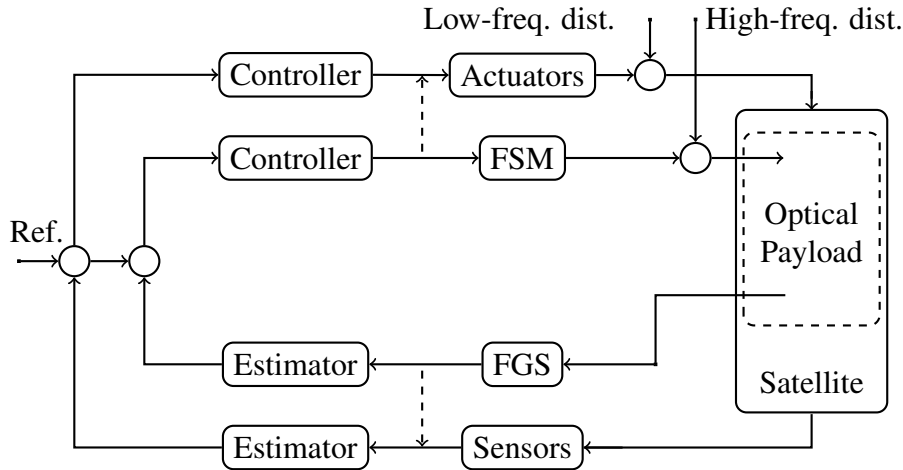


Figure 1: Control strategy of a spacecraft with both an ADCS and HPPP system. The dashed arrow below represents the potential use of FGS measurements within the ADCS estimator, as explained in section 2.4, while the dashed arrow on top represents the potential control interaction between both attitude and FSM controller, as explained in section 2.5.

### 1.3 Paper overview

The remaining content of the paper is divided into two main parts: section 2 elaborating on an astronomy mission called CubeSpec, and section 3 elaborating on a virtual EO mission for which new technologies are being researched within the framework of a project called AQUALIS. For both sections, the high-precision pointing platform is discussed and time-domain simulations are evaluated. Section 4 concludes the paper.

## 2 SIMULATION OF A HIGH-PRECISION POINTING ASTRONOMY MISSION

CubeSpec is a 6U astronomy CubeSat developed within the In-Orbit-Demonstration (IOD) program from ESA and funded by the Belgian Science Policy office (BELSPO) [7]. During its mission CubeSpec will monitor the spectral lines of light emitted by massive stars during a few months. The high-cadence observation results, visible as deformations of the spectral lines, will allow scientists to learn more about the inner structure of those stars through asteroseismology. More mission details and scientific background can be found in [8]. This section will further introduce the CubeSpec platform and instrument, explain the pointing performance requirements, elaborate on the simulation models, and discuss on the obtained simulation results.

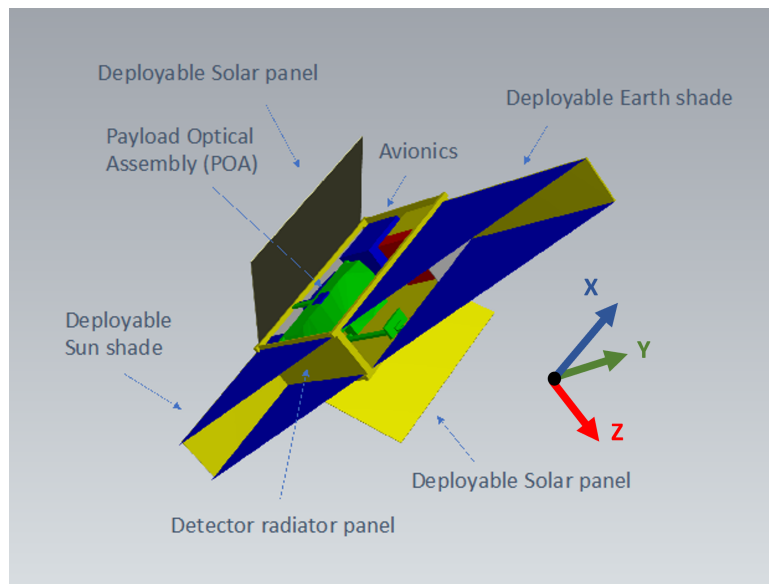


Figure 2: The CubeSpec platform with the payload, avionics and deployable panels clearly visible [9].

## 2.1 Overview of the CubeSpec platform and instrument

Figure 2 illustrates the CubeSpec platform after deployment. It is a 6U CubeSat platform ( $30 \times 20 \times 10 \text{ cm}^3$ ), of which four units (4U) are allocated to the optical payload and the remaining two units (2U) to the spacecraft bus and payload electronics. Deployable Sun- and Earth-shields protect the payload detector from unwanted illumination and heating, while solar panels deployed under  $45^\circ$  foresee the required power [9]. The payload instrument itself is composed of a 1.6 m focal length Cassegrain telescope and high-resolution spectroscope. Figure 3 depicts the lay-out of the spectroscope, including the beam-steering mirror (i.e. FSM) and fine-guidance sensor (FGS) of the HPPP. The dichroic element acts as a wavelength-based beamsplitter, deviating one part of the light to the FGS and the remaining part to the spectroscope instrument. The instrument also includes a slit, a collimator, a cross-disperser, an echelle grating, a detector, and folding mirrors.

## 2.2 Pointing performance requirements

To ensure the functionality of the spectroscope instrument, the incoming light should pass through a  $20 \times 50 \mu\text{m}^2$  slit for more than 80% of the observation time of maximum 15 min. This scientific requirement is translated into more classical requirements on the rotation about the x-axis and z-axis of the spacecraft reference frame (see Figure 2) as follows [11]:

1. The APE on the payload boresight, using only the ADCS, shall be less than  $0.2^\circ$  half-cone angle. This requirement should be met for 99.7% ( $3\sigma$ ) of the time using the temporal statistical interpretation.
2. The RPE on the payload boresight, using only the ADCS, shall be less than 180 arcsec half-cone angle for a time window of 15 min. This requirement should be met for 99.7% ( $3\sigma$ ) of the time using the temporal statistical interpretation.
3. The APE about the x- and z-axis of the spacecraft reference frame, using both the ADCS and HPPP, shall be less than 4 arcsec and 1 arcsec half-cone angle respectively. This requirement should be met for 68% ( $1\sigma$ ) of the total observation time of 15 min using the temporal statistical interpretation.

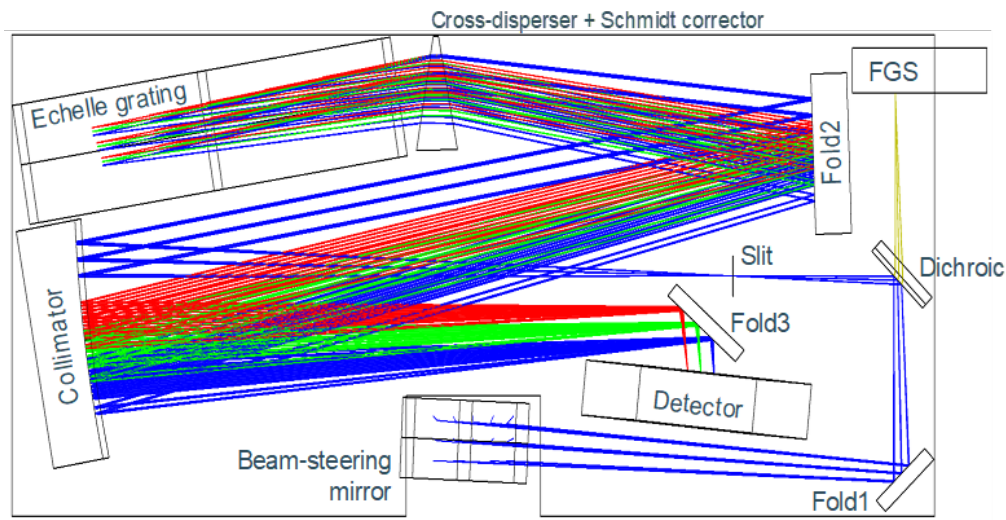


Figure 3: CubeSpec spectroscopy lay-out with the science instrument and HPPP components [10].

The first pointing requirement ensures that the observed star is always within the  $0.5^\circ$  telescope's field-of-view and is thus visible on the FGS. The second pointing requirement is derived from the kinematic and dynamic characteristics of the latest FSM design. The third and last pointing requirement is directly derived from the science requirement. Note that the value of the RPE on ADCS level highly interacts with the performance characteristics of the HPPP control loop.

### 2.3 Pointing performance simulation model

In order to evaluate the total pointing performance and the interactions between the different components, a Matlab/Simulink model of both the ADCS and HPPP is built according to Figure 1. While the pointing performance was already estimated within the Pointing Error Engineering Tool (PEET) in [11], this time-domain simulation model allows to include non-linearities and analyse transient behaviour. The simulations assume a three-axis stabilized 6U CubeSat in inertial high-precision pointing mode for which only the gyroscope, star tracker and three reaction wheels of the ADCS are assumed contributing to the stabilization of the platform. The gyroscope (GYR) parameters, of which the Angular Random Walk (ARW) and Rate Random Walk (RRW) are the main noise sources, are listed in Table 2. The star tracker (ST) parameter with the Near-Equivalent-Angle (NEA) as the main noise source is listed in Table 3 for cross-boresight and boresight ( $\cdot$ ). The reaction wheel simulation block includes a speed controller and a disturbance block, which produces force and torque noise in the form of unbalances, higher-order bearing harmonics, and structural eigenmodes of the reaction wheel assembly [5]. The parameters of the reaction wheels (RW) are listed in Table 4.

Within the HPPP control loop, the FGS measures the position (or centroid) of the observed star by means of a centroiding algorithm for which both the Gaussian-Grid and Center-of-Gravity algorithms are considered [12]. The FGS can then estimate the APE in two ways:

1. Through integrating the measured star positions. This method functions as long as the camera is affected by white Gaussian noise and the FSM is capable to reach its desired position before the next FGS measurement.
2. Through combining the measured star positions with strain gauge measurements to estimate the FSM position. The total noise variance on the APE then exists of the star position noise as well as the strain gauge position noise.

Table 2: GYR parameters

Parameter	Unit	Value
Maximum rate	[°/s]	±300
ARW ( $1\sigma$ )	[°/s <sup>1/2</sup> ]	$5 \cdot 10^{-3}$
RRW ( $1\sigma$ )	[°/s <sup>3/2</sup> ]	$1 \cdot 10^{-4}$
Quantization bits	[-]	16
Bandwidth	[Hz]	200

Table 3: ST parameters

Parameter	Unit	Value
NEA ( $1\sigma$ )	[arcsec]	10 (50)

Table 5: FGS parameters

Parameter	Unit	Value
NEA ( $1\sigma$ )	[arcsec]	0.1

Table 6: SG parameters

Parameter	Unit	Value
Maximum range	[mrad]	±3
Noise ( $1\sigma$ )	[μrad]	3
Quantization bits	[-]	16

Table 4: RW parameters

Parameter	Unit	Value
Static unbalance	[g mm]	0.5
Dynamic unbalance	[g mm <sup>2</sup> ]	20
Number of harmonics	[-]	11
Maximum speed	[rpm]	5000
Maximum torque	[mN m]	0.7
Quantization bits	[-]	16
Radial eigenmode	[Hz]	300
Axial eigenmode	[Hz]	600
Rotational eigenmode	[Hz]	100

Table 7: FSM parameters

Parameter	Unit	Value
Maximum range	[mrad]	±3
Noise ( $1\sigma$ )	[μrad]	15
Eigenfrequencies	[Hz]	400, 1040
Quantization bits	[-]	16
Distance to FGS	[mm]	158

The estimated pointing error is translated into a desired FSM position. The FSM simulation block takes into account the dynamics of the latest FSM design. Due to the strict dimensional limitations the FSM is in-house developed. Its design exits of three amplified piezo-electric actuators connected to a  $16 \times 36 \text{ mm}^2$  mirror through thin metal rods. The FSM dynamic model is a combination of second-order mass-damper-spring systems which account for the first mirror eigenmodes around both rotation axes and the actuator mode. Finite element analyses and eigenmode measurements show a good similarity between analyses and tests. At moment of writing, characterisation tests are being performed to obtain a final dynamic model.

The desired FSM position is translated into control voltages which pass two notch filters with center frequencies around the measured eigenfrequencies. Furthermore the FSM has its own feedback loop, with FSM position feedback measured with strain gauges attached to the actuators. This allows for higher control rates and shorter settling times. The FSM has a peak-to-peak reach of 6 mrad along both axes. The fine-guidance sensor (FGS), strain gauge (SG), and fine-steering mirror (FSM) parameters are listed in Tables 5, 6, and 7 respectively.

## 2.4 Pointing performance simulation results

Three scenarios are simulated, as listed in Table 8. In scenario 1 the HPPP and ADCS coexist without any communication in between, while in scenario 2 and 3 the FGS measurements are forwarded to the

Table 8: Overview of the different simulation scenarios.

Scenario	ADCS & HPPP communication	APE calculation method
1	(none)	Integrating (Method 1)
2	FGS exchange	Integrating (Method 1)
3	FGS exchange + FF control	FGS + SG (Method 2)

Table 9: Overview of the pointing performance simulation results for a time window of 15 min.

Scenario	Light within slit over time [%]	Axis	ADCS RPE ( $3\sigma$ ) [arcsec]	HPPP AKE ( $1\sigma$ ) [arcsec]	HPPP APE ( $1\sigma$ ) [arcsec]
1	53.9	x	207	8.3	59.7
		y	218	21.1	-
		z	215	8.0	47.1
2	60.7	x	178	1.3	49.0
		y	229	21.2	-
		z	192	1.0	40.0
3	67.0	x	180	1.3	39.7
		y	205	21.0	-
		z	210	1.0	29.4

ADCS estimator to improve the attitude estimation (see dashed arrow below in Figure 1). In scenario 3 there is also a feed-forward (FF) control included, which estimates the pointing error of the next step based on a quadratic function fitted on the last three samples.

The simulation results for the three different scenarios are listed in Table 9 and also visualized in Figure 4. The main performance parameters are the overall HPPP APE ( $1\sigma$ ) and the percentage of samples within the slit over a time window equal to the 15 min observation time. Note that the y-axis of the spacecraft reference frame corresponds to the boresight of the payload optics as well as the star tracker (see also in Figure 2).

From the results listed in Table 9 and Figure 4, following conclusions can be stated:

- The addition of the FGS measurements in the ADCS estimator in scenario 2 and 3 improves the HPPP AKE around the x- and z-axis with a factor 8, as compared to scenario 1.
- The feed-forward controller in scenario 3 improves both the percentage of light within slit as well the HPPP APE as compared to scenario 2.
- In scenario 1, the FSM is often saturated on one or two axes, which results in a cross pattern as illustrated in Figure 4a. By improving the HPPP knowledge with the FGS measurements exchange and feed-forward control as in scenario 3, the FSM is more relaxed, as illustrated in Figure 4b.
- The ADCS RPE simulations results are close to the ADCS RPE requirement (2), while the HPPP APE simulations results are still an order of magnitude too large as compared to the HPPP APE requirement (3).

Over the entire observation period of 15 min, it is expected that the RWs will change their wheel speed over a significant range. All simulations omit environmental torques, but an external torque was applied to see the effect of reaction wheel speed on the pointing performance. Figure 5 shows

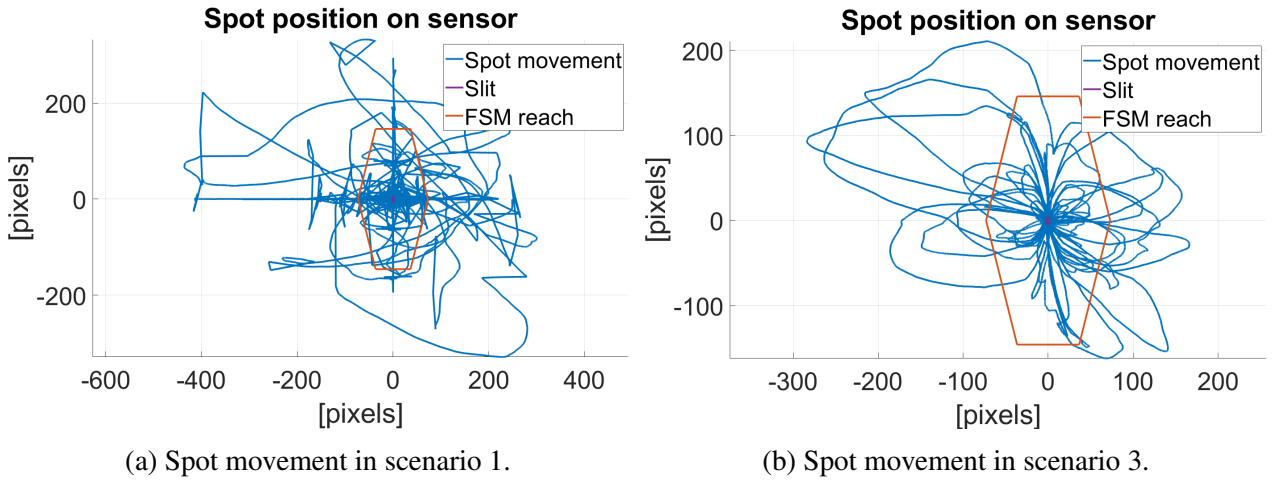


Figure 4: Spot movement during one simulation of 15 min. The red box indicates the FSM reach, the purple box indicates the slit.

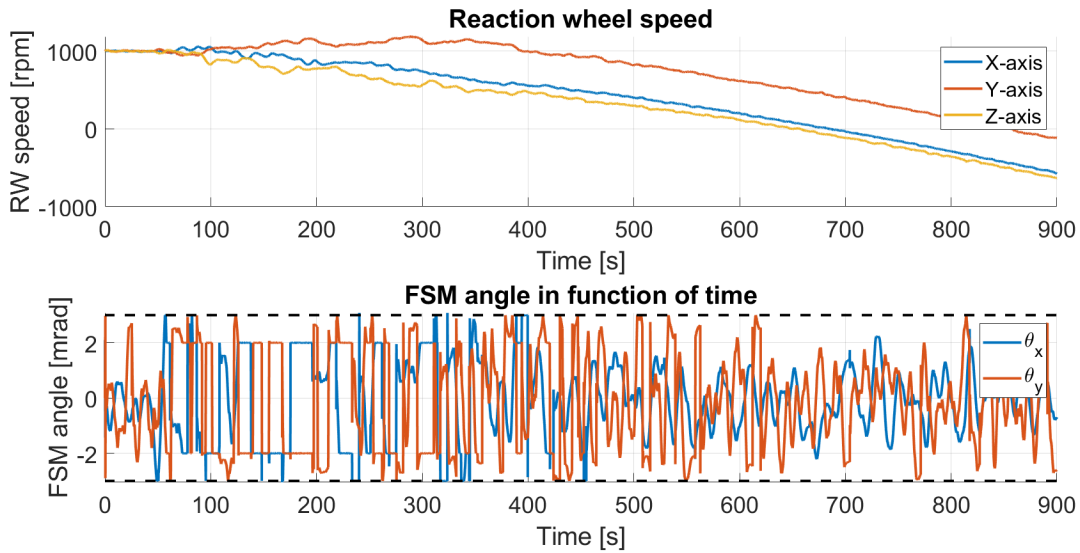


Figure 5: RW speed and FSM mirror position for scenario 1. The regions with constant FSM angles indicate FSM saturation where the it can no longer compensate the disturbances.

the RW speed and FSM position over time for scenario 1. At the start of the simulation, when the RW speeds are around 1000 rpm, the FSM is most of the time saturated, due to the high unbalance disturbances. After 600s, the RW speed is close to 0 rpm, during which the FSM is almost not saturated anymore. Unfortunately, RW zero-crossings should be avoided from operational point of view.

## 2.5 Future work

The proposed dual-stage approach for the CubeSpec mission is required to achieve the high-pointing precision in the range of a few arcsec, as stated in section 2.2. Although the HPPP inevitably adds complexity to the overall pointing system, the pointing performance can be increased by 33% around the x-axis (with the lowest inertia) and 57% around the z-axis. Nevertheless, additional improvements needs to be considered to further increase the pointing performance:

- The bandwidth of the attitude controller and FSM controller should be defined such that they

do not overlap, or even worse, counteract each other. This needs to be investigated.

- The HPPP controller can request more RW torque from the attitude controller to avoid saturation of the FSM (as illustrated by the dashed arrow on the top of Figure 1).
- A shift towards four reaction wheels instead of three could create more freedom to avoid or minimize the RW micro-vibrations by controlling their speed.
- A gyroscope with lower ARW noise would be beneficial. A gyro-less estimator instead of a gyro-stellar estimator, as proposed in [4], can be considered in high-precision pointing mode to neglect the high gyroscope noise.

### 3 SIMULATION OF A HIGH-PRECISION POINTING EO MISSION

The dual-stage approach can also be applied for Earth Observation (EO) missions. There are, however, some crucial differences with respect to astronomy missions regarding required pointing performance. First, the spacecraft does not operate in the inertial pointing mode, but in the more demanding Earth pointing mode (which requires a slow continuous rotation around one of the spacecraft axes). Secondly, the optical payload is not observing a celestial object as a point source, but the Earth scenery. Therefore, the FGS principle as discussed in section 2.3 is not applicable anymore. Yet, in order to merge the trend of small satellites and the demand of high-resolution EO images, this section will discuss the potential use of a dual-stage approach for EO missions on small satellite platforms. This research is part of the Affordable QUALity Images from Space (AQUALIS) project, which will be briefly explained in section 3.1.

#### 3.1 Overview of the AQUALIS project

The AQUALIS project is a strategic basic research (SBO) project, funded by the Flemish Research Foundation (FWO) and carried out by a consortium consisting of KU Leuven, VITO and imec [13]. The project goal is to develop and demonstrate innovative technologies which enable the acquisition of very high-resolution EO images from small platforms at reduced cost while maintaining high image quality, opening new possibilities in the new-space landscape. Within the AQUALIS project, three key technology blocks are developed to answer three main challenges:

1. Small spacecraft inherently have small optics with limited light gathering capabilities, leading to low signal-to-noise (S/N) ratios. The development of an advanced CCD-in-CMOS Time-Delay Integration line-scan camera allows to obtain higher S/N ratios.
2. Small spacecraft inherently have low moments of inertia and attitude control systems with limited stability performance, leading to image blur and geometrical shifts. The development of a high-precision pointing platform (HPPP) allows to improve the absolute and relative pointing performance.
3. Small spacecraft cannot accommodate advanced calibration devices that are tailored to their specific needs, characteristics and operation in constellations, leading to radiometrically poor data. Moreover, combining data from large constellations leads to different challenges in terms of data consistency (radiometric and spectral stability). The development of innovative image calibration algorithms allows to geometrically and radiometrically improve small satellite high-resolution EO data and make them consistent.

The following sections will elaborate on the research developments of technology block 2. For more information about the AQUALIS project, the reader is referred to [13].

### 3.2 Pointing performance simulation approach

Contrary to the CubeSpec mission, the AQUALIS project aims to develop technologies for small spacecraft platforms in general, without referring to a specific spacecraft design or mission. Therefore, the following approach is applied in order to perform different analyses on HPPP level:

1. First, a *baseline* mission and spacecraft design is defined, with the following starting assumptions: the CCD-in-CMOS TDI line-scan camera is the main optical payload; the satellite will be placed in a typical EO 500 km and 98° inclination orbit; and a ground-sampling distance (GSD) of 1 m is targeted. From these inputs, the size of the optics and spacecraft are estimated based on the calculations in [14]. The input and output parameters from these calculations are listed in Table 10. Note that upcoming technologies such as deployable optics and Ku-band (or laser) communication for CubeSats are assumed to be matured.
2. Secondly, the ADCS configuration and its performance is estimated based on the spacecraft size. Here, similar component performances (although slightly improved due to the different spacecraft platform size: 6U vs 24U) as listed in Tables 2, 3, 4 are considered.
3. Next, a pointing performance frequency-domain simulation is performed within PEET. The power spectral density (PSD) plot of the ADCS APE is then turned into random time series by means of an inverse Fast-Fourier Transform (ifft).
4. Finally, the ADCS APE time series are used as an input/error source within the HPPP time-domain simulations. The HPPP will thus try to correct the remaining ADCS errors (without any interaction). Only the inner control stage of Figure 1 is thus simulated.

The main reason for action 3 and 4 (i.e. excluding the ADCS from the time-domain simulations) is twofold: (1) an ADCS PEET model was already available from previous analyses [11], allowing to obtain some first results swiftly and (2), the time-domain HPPP simulations would require less computational effort without the ADCS stage.

Table 10: Mission & spacecraft parameters.

Parameter	Unit	Value
Orbit altitude	[km]	500
Orbit inclination	[°]	98
CubeSat platform	[U]	24
Focal length optics	[m]	2.7
Diameter optics	[m]	0.3
Downlink data rate	[Mbps]	350
Solar power generation	[W]	60

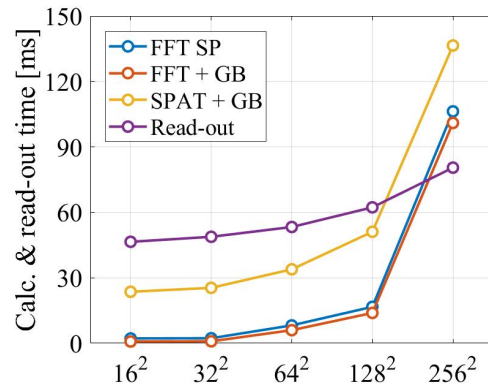


Figure 6: Calculation and read-out time in function of the size of ROI and algorithm. (Results are obtained with Python 3.8 on a HP Elitebook 840 G6 with Intel Core i7-8665U processor and 32GB RAM)

### 3.3 Pointing performance simulation model

The simulation model is very similar to the one described in section 2.3 although without the ADCS control loop. Furthermore, a COTS FSM [17], of which the parameters are listed in Table 13, is con-

Table 11: TDI camera parameters [15]

Parameter	Unit	Value
Pixel width	[ $\mu\text{m}/\text{pix}$ ]	5.4
Read-out frequency	[kHz]	7.06
Pixels per row	[pix]	4096
TDI stages per band	[-]	256

Table 12: ARS parameters [16]

Parameter	Unit	Value
Maximum rate	[ $^\circ/\text{s}$ ]	$\pm 5$
ARW	[ $^\circ/\text{s}^{1/2}$ ]	$4 \cdot 10^{-6}$
RRW	[ $^\circ/\text{s}^{3/2}$ ]	$8 \cdot 10^{-5}$
Quantization bits	[-]	16
Bandwidth	[Hz]	1000

Table 13: FSM parameters [17]

Parameter	Unit	Value
Maximum range	[mrad]	$\pm 5$
Bandwidth	[Hz]	150
Damping	[-]	0.7
Noise ( $1\sigma$ )	[ $\mu\text{rad}$ ]	3
Quantization bits	[-]	18
Distance to FGS	[mm]	300

Table 14: GCP parameters.

Parameter	Unit	Value
Distribution	[km]	IG(50, 20)
Noise ( $1\sigma$ )	[pix]	0.3
Loss	[%]	50

sidered which could fit within the baseline spacecraft design. The FSM is modelled as a closed-loop system of which the step response has a 1% settling time of 10 ms. The FGS is replaced by the TDI camera of which the main parameters are listed in Table 11. The idea is to use the TDI camera line-scans to assemble images and applying a correlation algorithm on two consecutive images to calculate the image shift in between them. This shift is a measure of the relative motion of the spacecraft. To validate the addition of the image shift calculations, an augmented EKF was developed which takes into account the noise of the TDI measurements. An independent correlation algorithm analysis is further explained in section 3.3.1.

Additionally, the potential use of onboard Ground Control Point (GCP) calculations for absolute pointing measurements is added. This addition assumes the spacecraft has a GCP catalogue onboard which can be consulted to offset any drifts originating from the rate sensor and/or TDI camera output (similar to what a star tracker does with a star catalogue). For the GCP modelling, an inverse Gaussian (IG) distribution with  $\mu = 50$  km and  $\lambda = 20$  km is assumed for the distance between two consecutive GCPs along-track. These distances are translated in sampling times by means of the satellite's ground velocity of 7.06 km/s. Moreover, a loss ratio of 50% was assumed to take into account failed GCP calculations and/or cloud coverage. Table 14 summarises the GCP parameters.

Finally, a (more exotic) angular rate sensor (ARS) based on the magneto-hydrodynamic principle is considered as this rate sensor has very low ARW noise characteristics [16] (Table 12) as compared to the typical low-cost MEMS Coriolis vibratory gyroscope (Table 2).

### 3.3.1 Image correlation algorithm analysis

Figure 7 illustrates the flow diagram of the correlation algorithm analysis that is performed to validate the image shift calculation time, rejection ratio, and accuracy. Several images with different scenes (representing different contrast levels) are taken as input. After selection of the Region-Of-Interest (ROI), three different correlation algorithms are applied [20]: (1) the spatial (SPAT) algorithm on pixel level in combination with the Gradient-Based (GB) algorithm, (2) the Fast-Fourier Transform (FFT) algorithm on pixel level in combination with the Gradient-Based (GB) algorithm, and (3) the Fast-Fourier Transform algorithm on subpixel level (FFT SP). Finally, each calculated shift was subjected

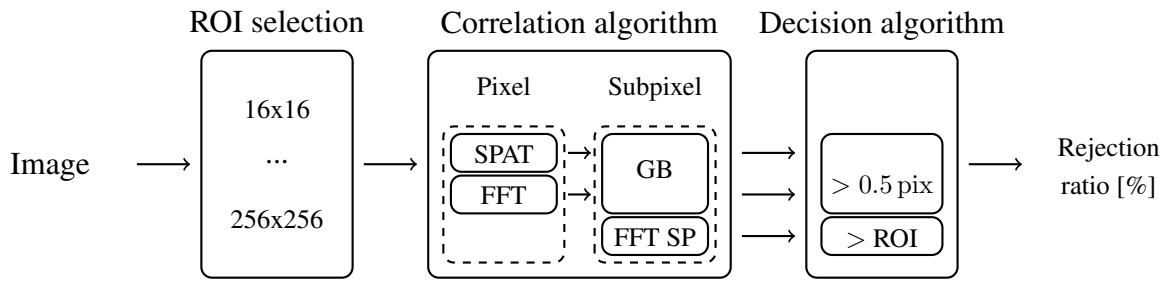


Figure 7: Flow diagram of the correlation algorithm analysis



(a) Desert [18]

(b) City [19]

(c) *Blurred* city [19]

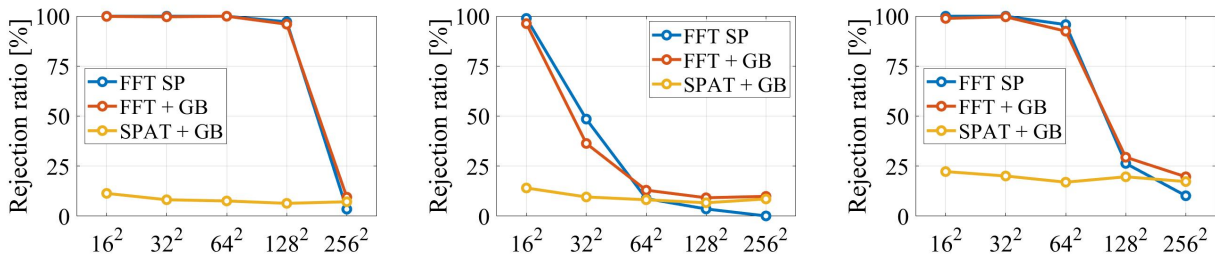


Figure 8: (Top row) Example images used for the correlation algorithm analysis. The *blurred* city image embodies a 30 pix TDI-shift. (Bottom row) The rejection ratio corresponding to the image above in function of the region of interest (ROI) size [pix<sup>2</sup>] and correlation algorithm.

to a specific decision algorithm to accept or reject the value. For the analysis, the decision value of the FFT SP algorithm is fixed, although this value can be estimated by means of GYR measurements. The top row of Figure 8 shows a desert image (low contrast), a city image (high contrast) and a city image with an internal TDI-shift of 30 pix (medium contrast). On the bottom row of Figure 8 the rejection ratio results of the correlation algorithm analysis are illustrated for each corresponding image above. As expected, the larger the ROI and the higher the contrast in the image scene, the lower the rejection ratio. The SPAT+GB algorithm combination outperforms the FFT-based algorithms as long as the ROI is smaller than  $256 \times 256 \text{ pix}^2$ . Though, the SPAT+GB algorithm combination requires more calculation time, as illustrated in Figure 6, which impacts the maximum sample frequency of the HPPP control loop. In case of acceptance, the  $1\sigma$  error of the image shift was in the order of 0.2 pix. The results of the image correlation analysis are directly implemented in the overall HPPP simulation.

### 3.4 Pointing performance simulation results

To evaluate the different sensor(s) (configurations) from previous section, several scenarios are defined according to Table 15. For the TDI camera, rather desert images in combination with a 16 pix ROI or city images in combination with a 32 pix ROI are assumed. The first option corresponds to a high rejection ratio but high sampling frequency; the second option vice versa. Table 16 shows the pointing performance metrics for each scenario. The RPE is given for a 75 ms time window which

Table 15: Overview of the different scenario's an EO mission.

Scenario	Sensors	Image	ROI [pix <sup>2</sup> ]	Corr. algorithm	Rejection ratio [%]	HPPP sampl. freq. [Hz]
1	ST+GYR	-	-	-	-	-
2	ST+GYR+CAM	Desert	16	FFT+GB	98	75
3	ST+GYR+CAM	City	32	SPAT+GB	11	20
4	ST+GYR+CAM+GCP	City	32	SPAT+GB	11	20
5	ST+ARS	-	-	-	-	-
6	ST+ARS+CAM	Desert	16	FFT+GB	98	75
7	ST+ARS+CAM	City	32	SPAT+GB	11	20
8	ST+ARS+CAM+GCP	City	32	SPAT+GB	11	20

corresponds to an image size of  $256 \times 4096$  pix<sup>2</sup>. From these results, following conclusions can be made:

1. The APE values are again in the same order as compared to the ones obtained for the CubeSpec simulations in section 2.4 although slightly better due to the larger platform and better sensor characteristics assumed here.
2. The RPE values are very low for a CubeSat platform, yet, only for a 75 ms time window, which was set as a reference in the project. Note that, due to the long focal length of the optics assumed, 1 pix corresponds to 0.4 arcsec. The RPE spans thus multiple pixels, resulting in potential blurry images.
3. The implementation of the TDI camera measurements in the augmented EKF deteriorates the AKE and APE instead of improving it. While the idea was to filter the TDI camera measurements based on their noise characteristics relative to the other sensor measurements (ST and GYR), the implementation of relative measurements do not work as it is now.
4. Although it is not noticeable from the standard deviation ( $1\sigma$ ) results, the potential use of GCPs prevents the gyroscope and/or TDI camera measurements from drifting. Otherwise, the star tracker is typically used as absolute pointing reference, although it has an insufficient accuracy for high-precision pointing applications towards 1 arcsec on small satellite platforms.

### 3.5 Future work

Due to the erroneous outcome of the TDI camera within the augmented EKF, future work mainly entails a review of its implementation. An alternative is a separate weighting filter on HPPP level. Next, the (idea of) GCP addition should be further elaborated. Also, the inclusion of the ADCS system as it is done in section 2 could be considered to take into account the change RW micro-vibrations. Finally, a parameter analysis can be performed to validate the sensor characteristics with respect to the pointing performance.

Alongside the simulations, the TDI camera read-out and FSM actuation is also being tested on a demonstration test setup [13] to validate the outcomes of the correlation algorithm analysis of section 3.3.1.

Table 16: Overview of the pointing performance simulation results for an EO mission over a time window of 10 min.

Scenario	HPPP AKE ( $1\sigma$ ) [arcsec]	HPPP APE ( $1\sigma$ ) [arcsec]	HPPP RPE [75 ms] ( $1\sigma$ ) [arcsec]
1	8.05	8.14	2.69
2	9.35	9.43	2.68
3	10.85	10.94	2.13
4	10.49	10.89	2.13
5	2.15	2.23	0.09
6	4.48	4.52	0.14
7	8.30	8.36	0.15
8	1.97	2.06	0.09

## 4 CONCLUSIONS

This paper started with a motivation and explanation of the dual-stage pointing control approach, called HPPP, which can improve current pointing performances of small satellites, based on the (optical) payload-in-the-loop principle. First, the HPPP configuration of CubeSpec, an astronomy mission, is being discussed, showing an improved pointing performance with 33 to 57% with respect to currently existing smallsat ADCS systems. Secondly, the HPPP approach of the AQUALIS project, in which innovative technologies for EO missions are being researched, is being revealed, showing again improved pointing performances, although the relative image correlation measurement implementation should be reviewed.

## REFERENCES

- [1] “CubeSat Desing Specification Rev. 14,” Cal Poly, San Luis Obispo, CA, Tech. Rep., 2020.
- [2] R. Shimmin, “Small Spacecraft Technology State of the Art,” NASA Ames Research Center, Tech. Rep., 2015.
- [3] European Cooperation for Space Standardization (ECSS), *Space Engineering - Control Performance (ECSS-E-ST-60-10C)*, [standard], 2008.
- [4] J. Vandersteen, J. Vennekens, and R. Walker, “Nano- to Small Satellite Pointing Errors: Limits of Performance,” in *Proc. of the Small Satellites, System and Services Symposium (4S)*, Valetta, Malta, 2016.
- [5] W. D. Munter, T. Winters, J. Lanting, T. Delabie, and D. Vandepitte, “Balancing method and experiment of a small spacecraft reaction wheel,” in *Proc. of the 29<sup>th</sup> international conference on noise and vibration engineering*, Leuven, Belgium, 2020, pp. 1481–1496.
- [6] T. Mladenov, “FPGA-based Active Pointing Correction of Optical Instruments on Small Satellites,” M.S. thesis, Dept. of Mech. Eng., KU Leuven, 2018.
- [7] G. Raskin, T. Delabie, W. D. Munter, *et al.*, “CUBESPEC: Low-cost space-based astronomical spectroscopy,” in *Proc. SPIE 10698, Space Telescopes and Instrumentation 2018: Optical, Infrared, and Millimeter Wave*, Austin, Texas (US), 2018. DOI: 10.1117/12.2314074.

- [8] D. M. Bowman, B. Vandenbussche, H. Sana, *et al.*, “The CubeSpec space mission. I. Asteroseismology of massive stars from time series optical spectroscopy: science requirements and target list prioritisation,” *Astronomy & Astrophysics*, vol. 658, 2022. DOI: 10.48550/ARXIV.1805.11848.
- [9] B. Vandenbussche, G. Raskin, P. Royer, *et al.*, “CubeSpec - Enabling spectroscopy from a CubeSat platform.” in *Proc. of the Small Satellites, System and Services Symposium (4S)*, Vilamoura, Portugal, 2022.
- [10] “CubeSpec - Enabling astronomical spectroscopy from a CubeSat platform.” Accessed on: 25-05-2023. (2022), [Online]. Available: <https://fys.kuleuven.be/ster/instruments/cubespec>.
- [11] W. D. Munter, “CubeSpec - Satellite Pointing Analysis Report (PDR),” 2020.
- [12] T. Delabie, “Star Tracker Algorithms and a Low-Cost Attitude Determination and Control System for Space Missions,” Ph.D. dissertation, KU Leuven, 2016.
- [13] W. D. Munter, J. D. Maeyer, L. Peri, D. Vandepitte, S. Livens, and S. Thys, “AQUALIS: Affordable Quality Images from Space,” in *Proc. of the 14<sup>th</sup> IAA Symposium on Small Satellites for Earth System Observation*, Berlin, Germany, 2023.
- [14] B. Chesley, R. Lutz, and R. Brodsky, “Space Payload Design and Sizing,” in *Space Mission Analysis and Design (SMAD)* (Space Technology Library), Space Technology Library. Microcosm Press and Kluwer Academic Publishers, 1999, ch. 9, pp. 241–300.
- [15] P. Boulenc, “Multi-spectral High-Speed Backside Illuminated TDI CCD-in-CMOS Imager,” in *International Image Sensor Workshop*, 2019.
- [16] BlueHalo, *ARS16 - Angular Rate Sensor*, [datasheet], 2021.
- [17] Cedrat Technologies, *Piezo Tip-Tilt (DTT60SM-SG)*, [datasheet], 2022.
- [18] Google Earth v.7.3.4.8248 (27/02/2011), *Arabian Desert: 29°31'8.42" N, 42°20'49.33" W, Alt 3.89 km*, Maxar Technologies, Accessed on: 29-03-2022.
- [19] Google Earth v.7.3.4.8248 (06/08/2020), *Paris: 48°52'41.55" N, 2°20'40.54" W, Alt 3.58 km*, Accessed on: 29-03-2022.
- [20] M. Guizar-Sicairos, S. T. Thurman, and J. R. Fienup, “Efficient subpixel image registration algorithms,” *Opt. Lett.*, vol. 33, no. 2, pp. 156–158, 2008. DOI: 10.1364/OL.33.000156.